Supporting Information

High-Performance p-Type Elemental Te Thermoelectric Materials Enabled by Synergy of Carrier Tuning and Phonon Engineering

Decheng An[a], Shaoping Chen[a,], Xin Zhai[a], Yuan Yu[c], Wenhao Fan[d], Tingting Zhang[e], Yequn Liu[f], Yucheng Wu[a], Wenxian Wang[a,]*, and G. Jeffrey Snyder[b,]**

[a] College of Materials Science and Engineering, Taiyuan University of Technology, Taiyuan 030024, P. R. China

[b] Department of Materials Science and Engineering, Northwestern University, Evanston, IL 60208, USA

[c] I. Physikalisches Institut (IA), RWTH Aachen University, Sommerfeldstraße, 52074 Aachen, Germany

[d] College of Physics and Optoelectronics, Taiyuan University of Technology, Taiyuan 030024, P. R. China

[e] Institute of Advanced Forming and Intelligent Equipment, Taiyuan University of Technology, Taiyuan 030024, P. R. China

[f] Analytical Instrumentation Center, State Key Laboratory of Coal Conversion, Institute of Coal Chemistry, Chinese Academy of Sciences, Taiyuan 030001, P. R. China

* Corresponding author E-mail address: sxchenshaoping@163.com (S. Chen), wangwenxian@tyut.edu.cn (W. Wang), jeff.snyder@northwestern.edu (G. J. Snyder)

1. Experimental Section

Materials fabrication: Polycrystalline $Te_{0.985}Sb_{0.015}$-x%$SmSe_2$ (x = 0, 0.5, 1, 1.5, 2, 3, and 4; x is in mole ratio), $Te_{1-x}Sm_x$ ($x \leq 0.01$) and $Te_{1-y}Sb_y$ ($y \leq 0.025$) samples were prepared by melting the stoichiometric compositions of high-purity elements Te (99.999%, Aladdin), Sb (99.999%, Aladdin), Sm (99.999%, Aladdin), and Se (99.999%, Aladdin), which were sealed in the graphite-coated quartz tubes under a vacuum (~10^{-4} torr). The raw materials were slowly raised to 1253 K in 10 h, then dwelled for 20 h, and subsequently quenched in cold water. After annealing at 723 K for 48 h, the obtained ingots were hand-ground into fine powders in an Argon-filled glove box and further consolidated using spark plasma sintering (SPS-331Lx, Japan) at 658 K for 8 min under a uniaxial pressure of ~50 MPa. Finally, dense sintered (>98% of theoretical density) cylinder-shaped pellets with a thickness of ~ 8 mm and a diameter of 17 mm were obtained.

Thermoelectric properties measurements: The electrical transport properties including electrical resistivity (ρ) and Seebeck coefficient (S) were measured on a Namicro-3L system in a high vacuum atmosphere from room temperature to 600 K. The typical dimensions of the required SPSed samples are about 2×2×8 mm^3. Heating and cooling cycles allow repeatable electrical transport properties for the synthesized products. The measuring uncertainty of ρ and S was ~ 5%. The Hall coefficient (R_H) was investigated under a reversible magnetic field (1.5 T) using the van der Pauw method across the temperature range of 300 K to 600 K during heating and cooling. The hole concentration (n_H) and Hall carrier mobility (μ_H) were determined according to the relations $n_H = 1/(eR_H)$ and $\mu_H = \sigma R_H$, respectively, where e represents the electron charge. The total thermal conductivity was calculated using $\kappa = D\rho C_p$, where the thermal diffusivity (D) was measured on a Netzsch LFA457 instrument by the laser flash method, the density (ρ) was estimated by the Archimedes principle (Table S1), and the specific heat capacity (C_p) was calculated according to the Dulong-Petit law, which was assumed to be temperature independent. Given the individual uncertainty of each parameter, the measurement uncertainty of thermal conductivity κ was estimated to be within 10%. The combined uncertainty for all measurements involved in zT determination is below 20%.

Materials characterizations: The phase compositions and crystal structure of all samples were identified through room-temperature powder X-ray diffraction (XRD) analysis (Ultima IV, Rigaku, Japan) using Cu K_α radiation (λ = 1.5418 Å, 40 kV, 40 mA), with a scan speed of 2°/min and a step size of 0.01°. In order to obtain the lattice parameter, the X-ray diffraction patterns were refined via FULLPROF software suite based on the Rietveld method. The X-ray photoelectron spectroscopy (XPS) were conducted on Thermo ESCALAB 250XI using Al K_α as the X-ray source (1486.74 eV) with energy resolution of 0.43 eV. The carbon 1s peak (binding energy 284.8 eV) was used as a reference to calibrate the binding energies of the other core level spectra. The fresh fracture morphologies and chemical compositions of fabricated samples were studied by scanning electron microscope (SEM, TESCAN MIRA3) equipped with an energy dispersive spectroscopy (EDS). The electron backscattered diffraction (EBSD) analysis was performed on a JEOL JSM-7800F system to characterize the crystalline orientation and crystal grain sizes. The specimens suitable for EBSD investigations were subjected to ion-beam etching. The EBSD maps were obtained by using the Oxford Instruments (OI) Channel 5 software. For transmission electron microscopy (TEM), the thin samples were prepared by conventional methods including cutting, grinding, dimpling, polishing and Ar ion-milling (Gatan PIPS Model691). The nanostructures of the specimens were analyzed on a JEM-2100F microscope equipped with an EDS detector at an accelerating voltage of 200 kV. Sound velocity measurements were performed on the SPSed pellets at room temperature to collected the transverse (v_t) and longitudinal (v_l) speed of sound, respectively. The sound speed data was obtained by use of ultrasonic pulser/receiver (OLYMPUS-5077PR) equipped with a digital oscilloscope (KEYSIGHT). The room-temperature elastic modulus, including shear modulus (G), bulk modulus (B), and Young's modulus (E), can be calculated from the above sound velocities by using the following equations [1-3]:

$$G = \rho v_t^2 \tag{1}$$

$$B = \rho\left(v_l^2 - \frac{4v_t^2}{3}\right) \tag{2}$$

$$E = \frac{9BG}{3B+G} = \frac{\rho v_t^2\left(3v_l^2 - 4v_t^2\right)}{\left(v_l^2 - v_t^2\right)} \tag{3}$$

The nano-mechanical properties of all bulk samples were measured in a Nanoindentation Agilent G200 Tester equipped with a standard Berkovich indenter with a load of 20 mN. Nano-hardness and Young's modulus were determined from the measured load versus depth curves under loading/unloading process. The nanoindentation tests were carried out 12 times for each sample (six times for matrix and second phase, respectively) to ensure the repeatability of the measuring data. The uncertainty in nanoindentation measurement is within 10%.

2. Rietveld refinements for $Te_{0.985}Sb_{0.015}$-x%$SmSe_2$

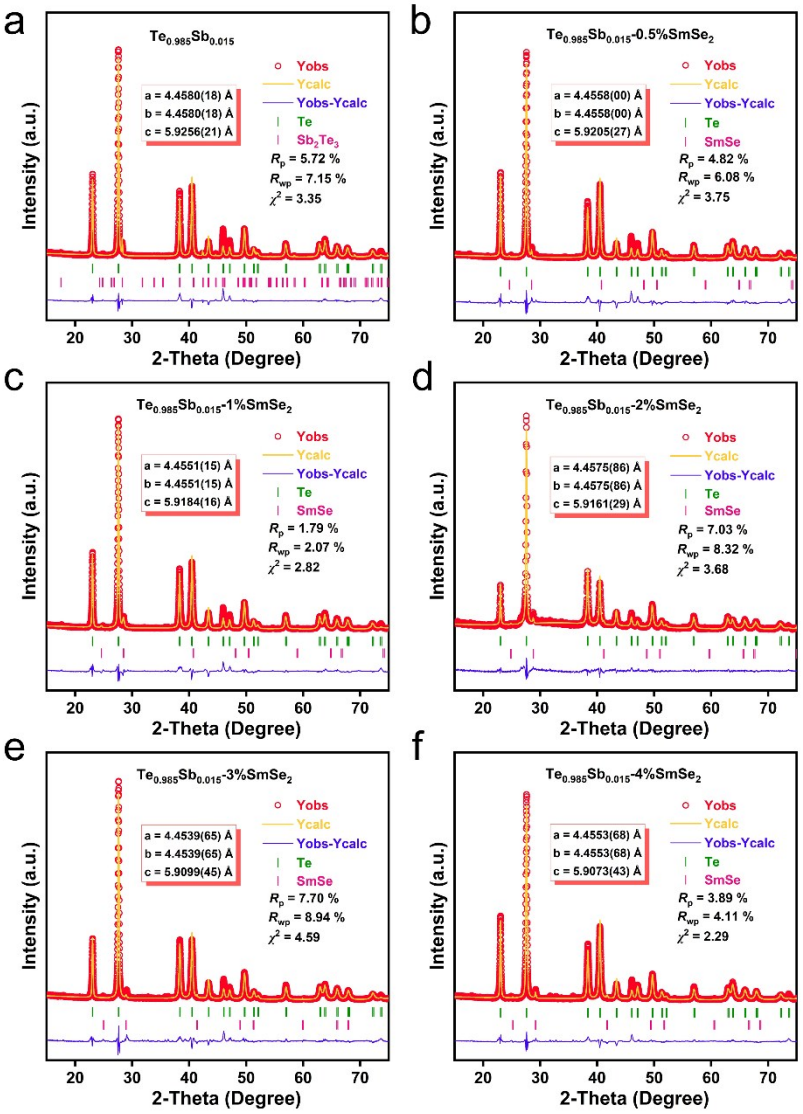

Figure S1. Rietveld refinement plots of $Te_{0.985}Sb_{0.015}$-x%$SmSe_2$ (x = 0, 0.5, 1, 2, 3, and 4) with the observed patterns in red, calculated patterns in yellow, and the differences between the observed and calculated intensities as a solid line at the bottom of the figure.

3. Compositional characterizations for synthesized samples

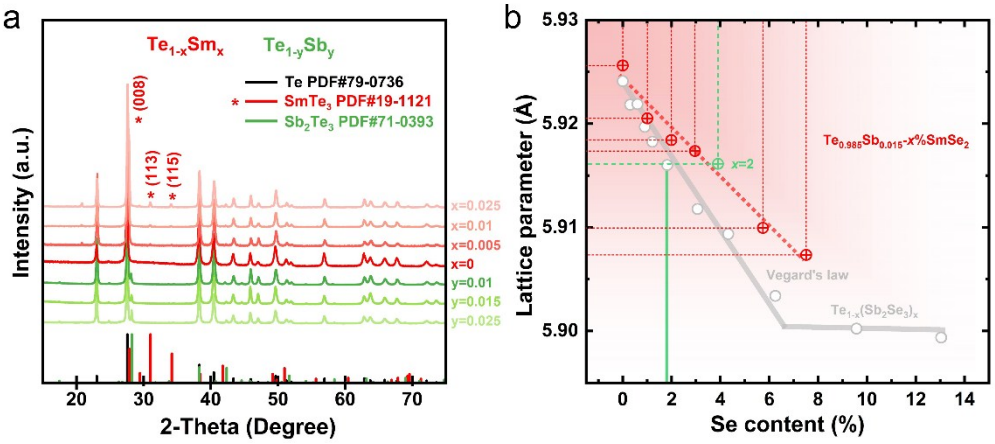

Figure S2. (a) XRD patterns for Sm-doped and Sb-doped Te, respectively. (b) The Se composition-dependent lattice parameter for $Te_{0.985}Sb_{0.015}$-x%$SmSe_2$ with a comparison to that of $Te_{1-x}(Sb_2Se_3)_x$. It is found that the main diffraction peaks correspond well to the trigonal Te, besides, there are additional weak peaks of $SmTe_3$ (corresponding to red lines) and Sb_2Te_3 (green lines) in patterns, separately. These impurities peaks suggests that the solubility limit of both Sm and Sb in Te is very limited (< 0.5 at.%), consistent with the previous reports [4, 5].

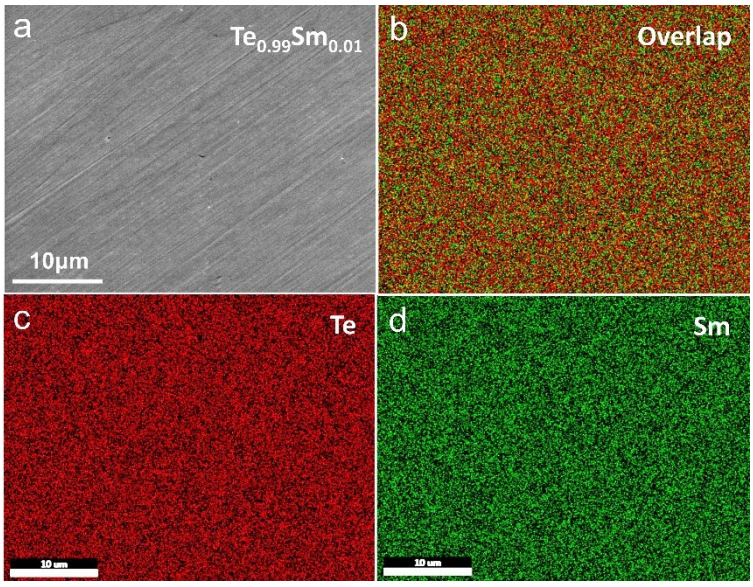

Figure S3. (a) Second electron images for $Te_{0.99}Sm_{0.01}$ pellet. (b–d) corresponding EDS mapping results for (a). All elements (Te and Sm) show a homogeneous distribution, indicating that Sm can be doped into the Te.

4. Electrical transport properties of Sm/Sb doped polycrystalline Te samples

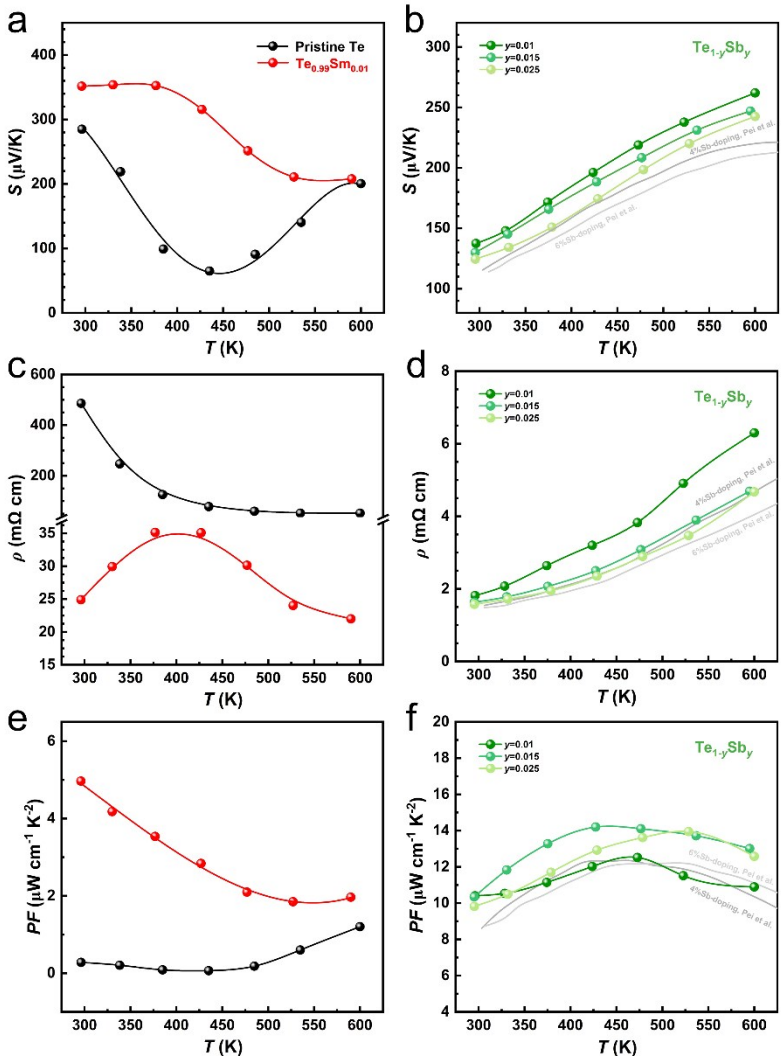

Figure S4. Temperature dependence of the electrical transport properties of synthesized Te products doped with Sm and Sb. (a, b) Seebeck coefficient, (c, d) electrical resistivity, and (e, f) power factor. Both samarium and antimony work as p-type dopants in tellurium. For Sm-doping Te sample, the Seebeck coefficient and electrical resistivity increase with increasing temperature up to T = 400 K, and afterward significantly decrease. These observations can be attributed to the bipolar effect deriving from thermal activation, suggesting Sm doping does not modify n_H notably. Generally, the relatively low n_H would lead to a strong bipolar behavior and a larger reduced Seebeck coefficient [5]. In this work, the

individual doping of Sb in Te is also discussed. As can be seen, both the Seebeck coefficient and electrical resistivity decrease upon increasing y, which is mainly caused by the significantly enhanced n_H due to Sb-doping. The integration of the reduced Seebeck coefficient and optimized electrical resistivity results in a highest PF of 14.2 μW cm^{-1} K^{-2} (at T = 425 K) for $Te_{0.985}Sb_{0.015}$ sample.

5. Thermal transport properties of $Te_{0.985}Sb_{0.015}$-x%$SmSe_2$ samples

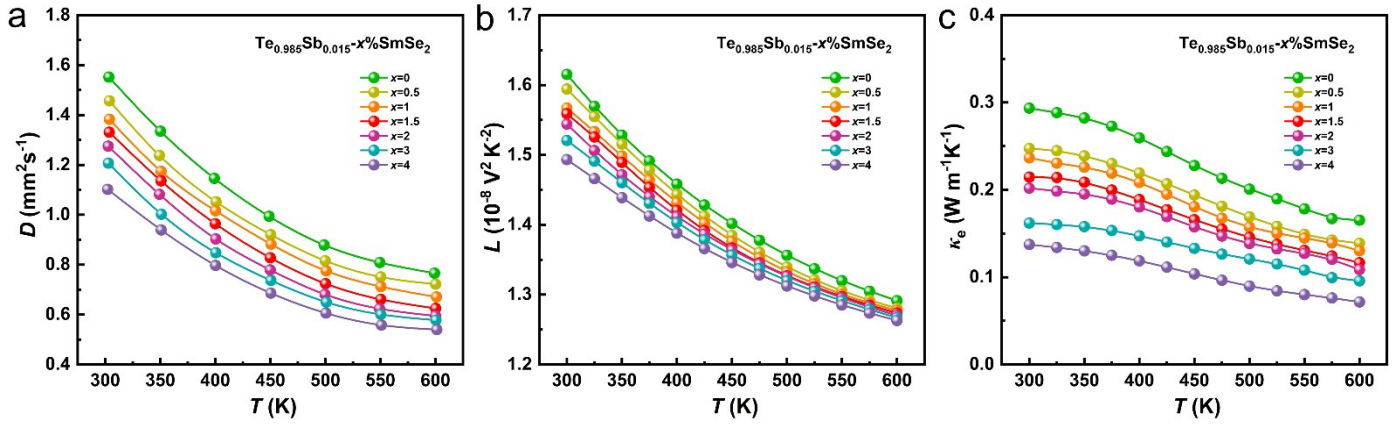

Figure S5. Temperature dependence of (a) thermal diffusivity (D), (b) Lorenz number (L), and (c) electrical thermal conductivity for $Te_{0.985}Sb_{0.015}$-x%$SmSe_2$ samples.

6. Compositional and morphological characterizations of $Te_{0.985}Sb_{0.015}$-x%$SmSe_2$ samples

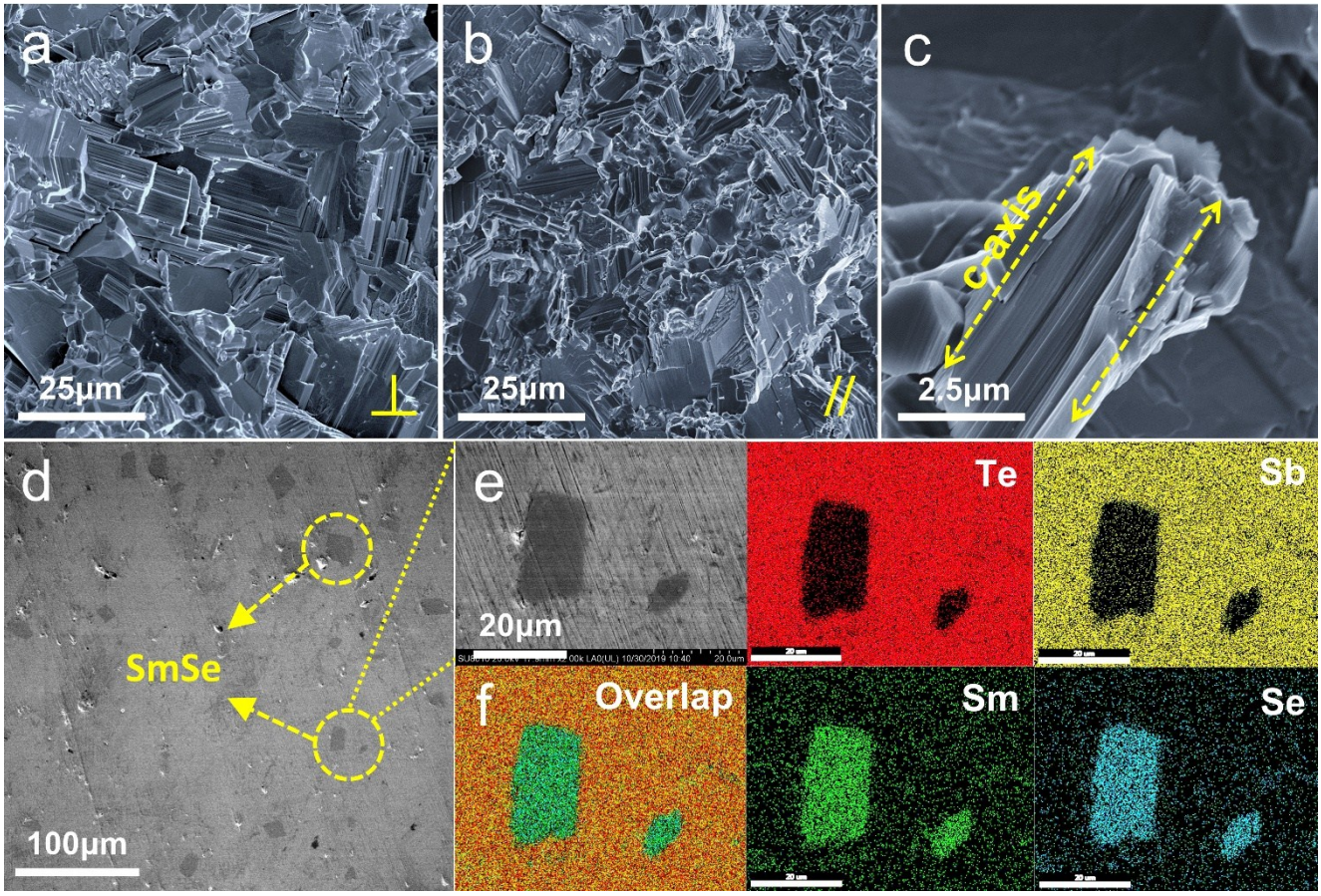

Figure S6. SEM images of fractured surface perpendicular (a) and parallel (b) the pressing directions for $Te_{0.985}Sb_{0.015}$-3%$SmSe_2$, respectively. (c) Enlarged view of the Te cleavage plane in (a) to see the quasi-one-dimensional structure. (d) Back-scattered electron image of polished surface for synthesized $Te_{0.985}Sb_{0.015}$-2%$SmSe_2$ sample. (e, f) corresponding EDS mapping taken from the marked region in (d) for Te, Sb, Sm, and Se.

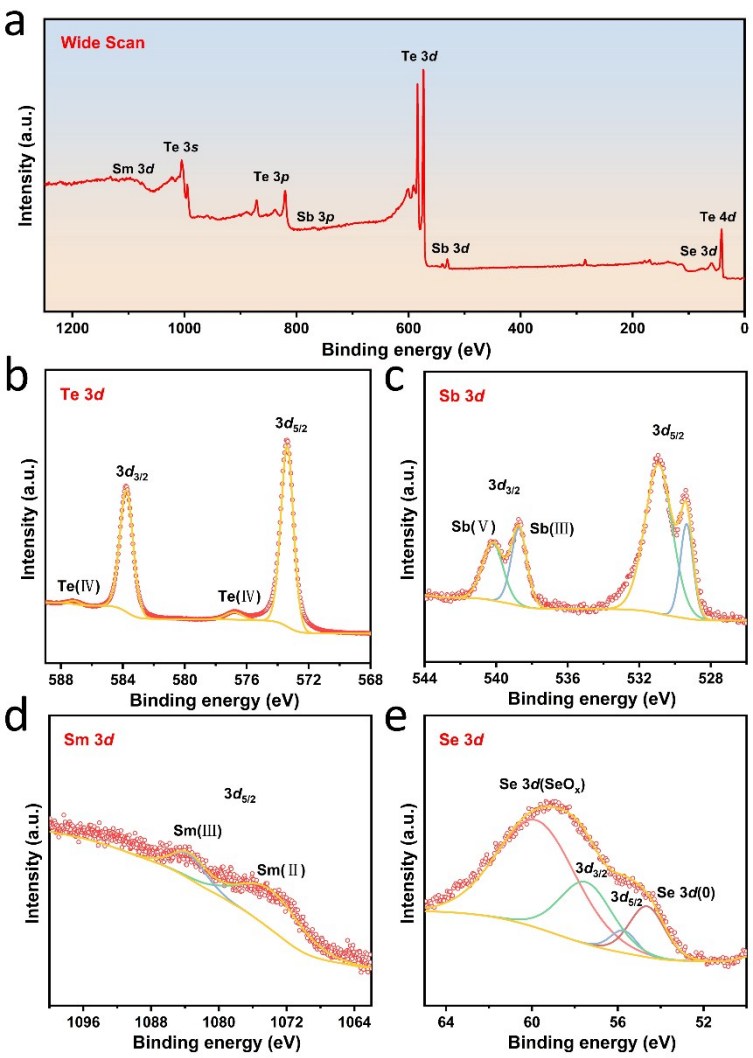

Figure S7. XPS survey spectra for $Te_{0.985}Sb_{0.015}$-2%$SmSe_2$ sample: (a) wide scan spectrum, high resolution scans of XPS spectra for the elements (b) Te 3d, (c) Sb 3d, (d) Sm 3d and (e) Se 3d. As can be seen, the Te 3d spectrum mainly exhibits two contributions, $3d_{3/2}$ and $3d_{5/2}$ (stemming from the spin-orbit splitting), located at 583.9 and 573.5 eV, characteristic of Te^{2-}. Additionally, small peaks at 587.2 and 576.8 eV alongside two Te 3d signals can be also observed, which is attributed to Te oxide. The Sb 3d spectrum is illustrated in Figure S7c. The peak centered at 539.1 eV corresponds to Sb(Ⅲ). In addition, binding energies of Sb $3d_{3/2}$ (540.2 eV) and Sb $3d_{5/2}$ (530.8 eV) are good agreement with reported values for an oxidation state of Sb(Ⅴ). The peaks of Sm $3d_{5/2}$ appear at 1083.3 eV for Sm(Ⅲ) and 1074.0 eV for Sm(Ⅱ) state. Se 3d(0) peak orbital appears at 54.9 eV, indicating that metallic Se element was alloyed into Te matrix.

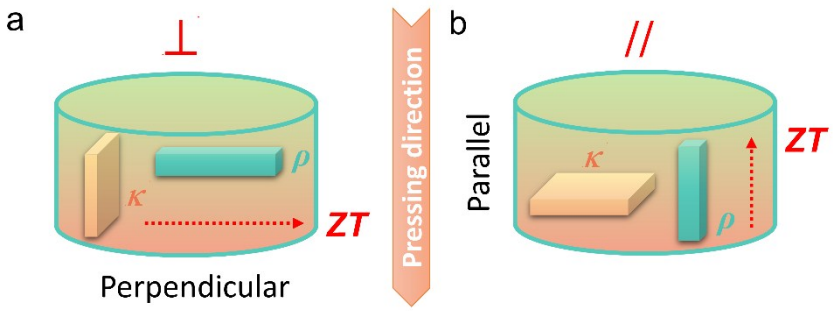

Figure S8. Schematic illustration of both the morphological and thermoelectric analyses performed from the perpendicular (a) and parallel (b) directions.

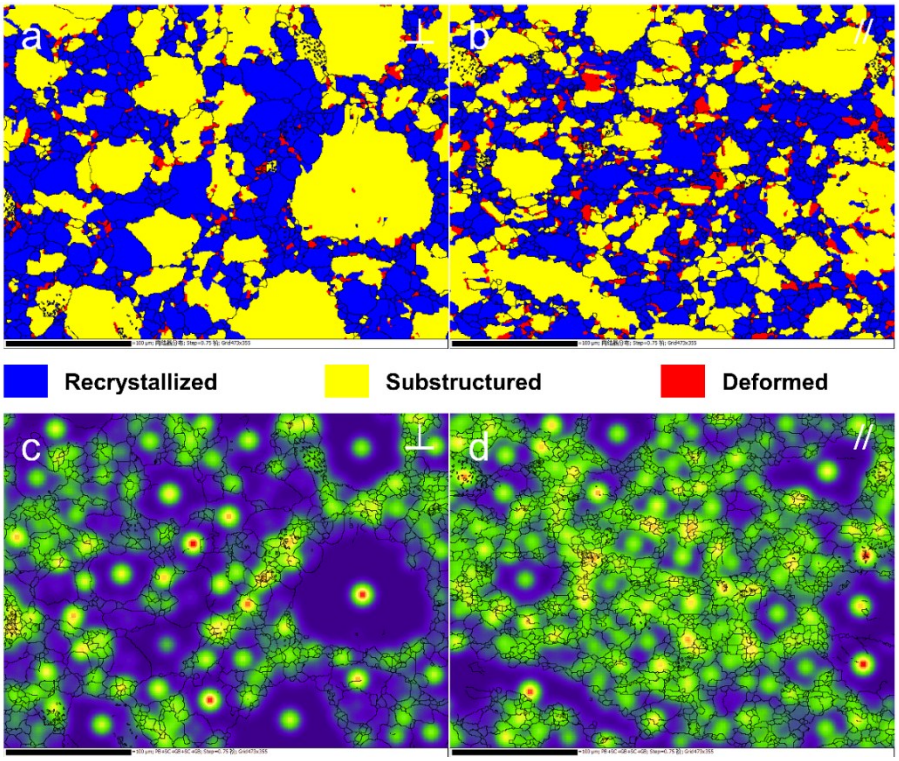

Figure S9. (a) EBSD maps distinguished recrystallized, substructured and deformed region taken from the perpendicular and parallel directions. (b) corresponding local strain distribution showing that the maximum strain distribution is located in the substructured region.

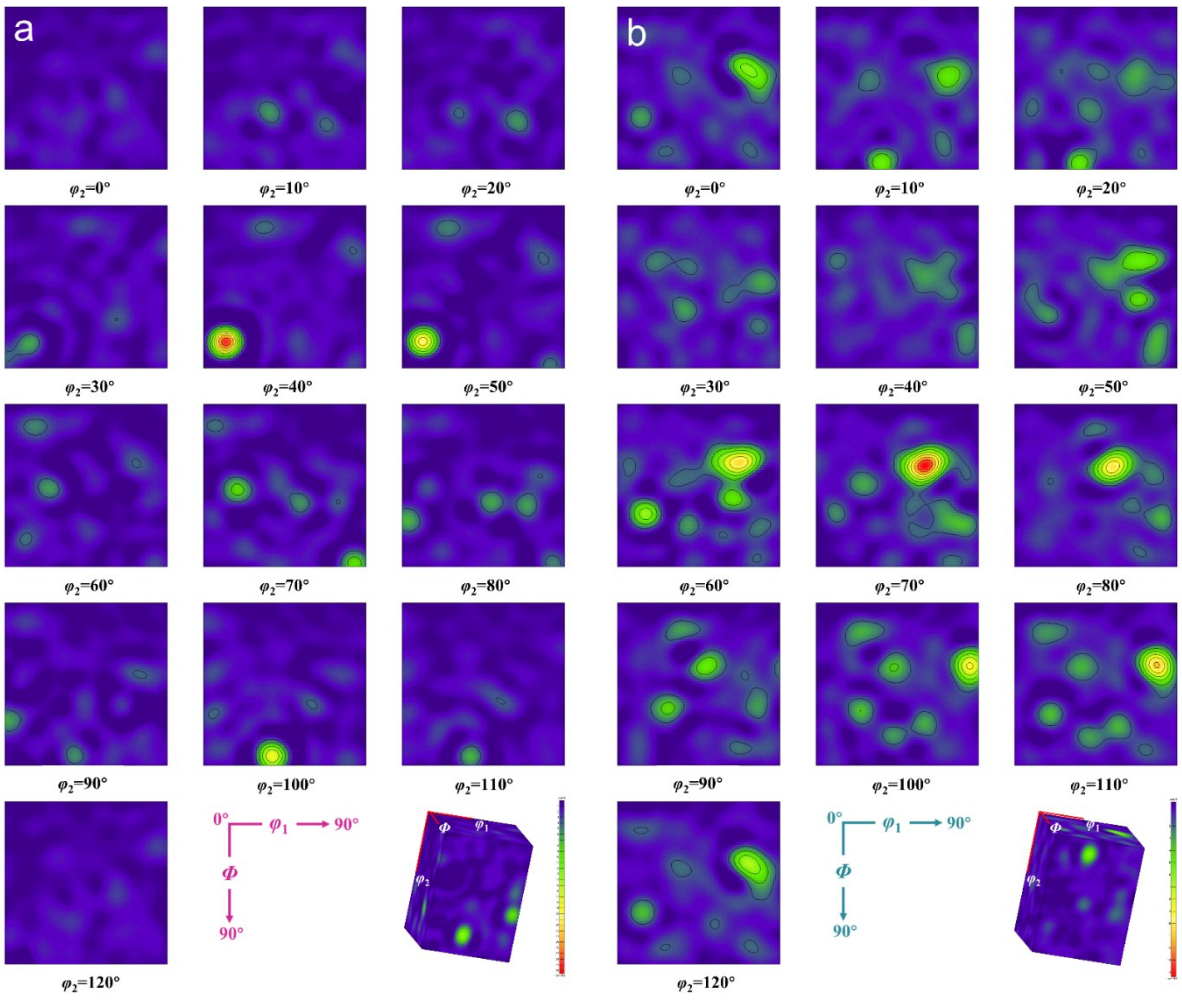

Figure S10. Orientation distribution function (ODF) patterns for the $Te_{0.985}Sb_{0.015}$-0.5%$SmSe_2$ sample along directions perpendicular (a) and parallel (b) to that of SPS pressure. Euler angle φ_2 is increased from 0° to 120° every 10 degrees.

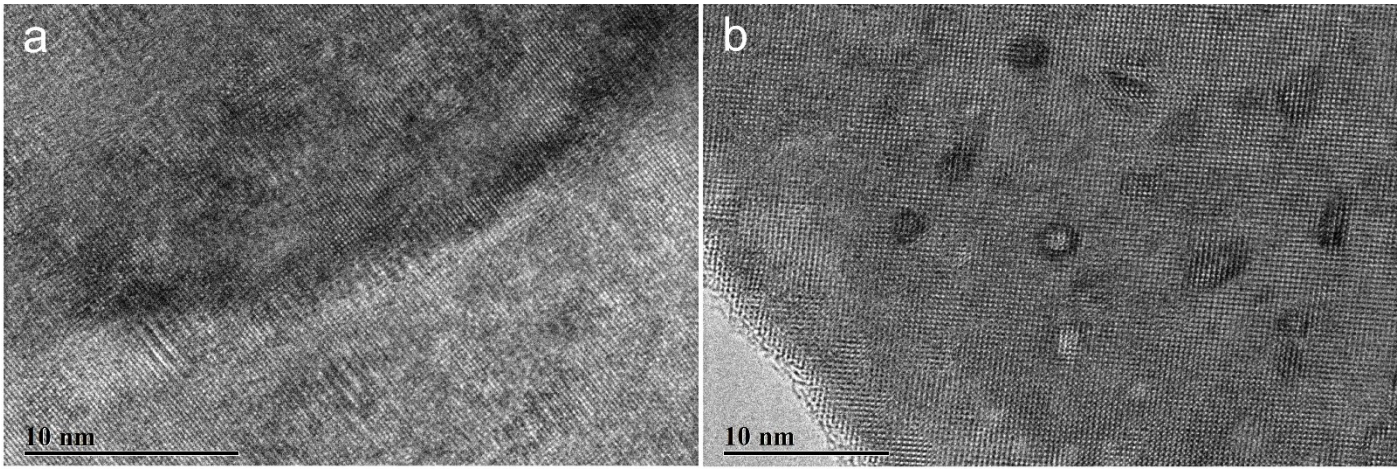

Figure S11. (a) An individual in-grain line defect embedded in the matrix. (b) HRTEM image along [$1\bar{1}0$] showing coherent interfaces.

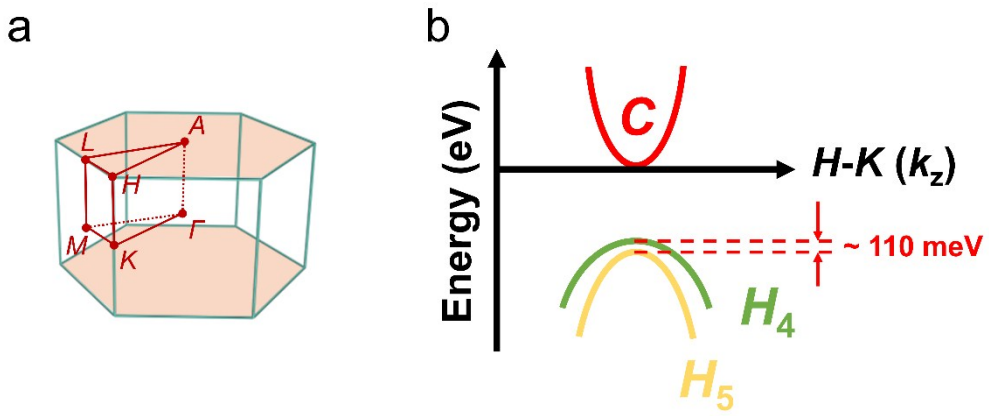

Figure S12. (a) Brillouin zone with high symmetry points. (b) Schematic diagram of valence band structure for Te. In view of a small band offset between the H_4 and H_5 valence bands, the nested valence bands can be approximated as an effective single band for simplicity [4]. In fact, the lower H_5 valence band close in energy to the upper H_4 valence band gives rise to the S-shape density of states at about 0.1 eV below the valence band maximum (VBM), which plays an important role in the transport properties [6].

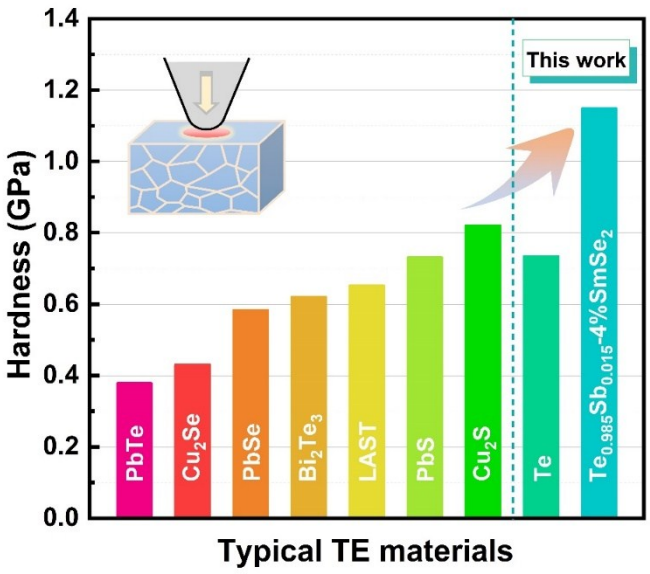

Figure S13. Indentation hardness at max load of pristine Te and $Te_{0.985}Sb_{0.015}$-4%$SmSe_2$ sintered pellets in comparison with other state-of-the-art TEs.

7. The repeatability of thermoelectric properties

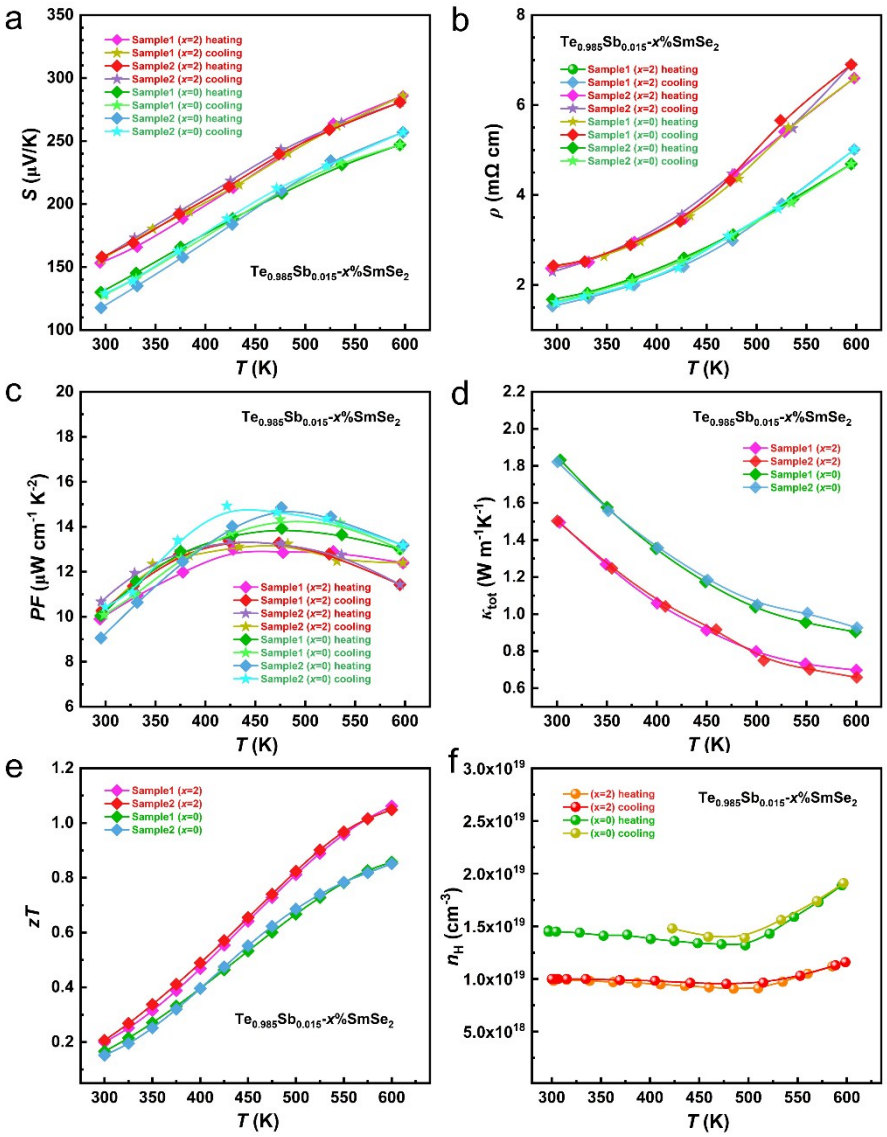

Figure S14. The repeated measurements of thermoelectric properties for $Te_{0.985}Sb_{0.015}$-x%$SmSe_2$ (x = 0, 2) from the ⊥ direction, showing a highly reproducible and stable performance. Temperature dependence of (a) Seebeck coefficient, (b) electrical resistivity, (c) power factor, (d) total thermal conductivity, (e) zT values, and (f) Hall carrier concentration. Note that all the samples are prepared with the same synthesis condition.

Table S1. The Seebeck coefficient (S), Hall carrier concentration (n_H), Hall carrier mobility (μ_H), electrical resistivity (ρ), lattice thermal conductivity (κ_L), deformation potential coefficient (Ξ), density of state effective mass (m^*_{DOS}), measure density (d), and relative density (%) of $Te_{0.985}Sb_{0.015}$-x%$SmSe_2$ system (x = 0 – 4) at both room temperature (300 K) and high temperature (600 K).

Composition	T (K)	S (μV K^{-1})	n_H (10^{18} cm^{-3})	μ_H (cm^2 V^{-1}s^{-1})	ρ (mΩ cm)	κ_L (W m^{-1}K^{-1})	Ξ (eV)	m^*_{DOS} (m_e)	Measured density (g cm^{-3})	Relative density (%)
x=0	300	132	14.49	261	1.65	1.56	27.96	0.46	6.18	99.0
x=0	600	248	19.22	69	4.75	0.74	10.67	0.75		
x=0.5	300	139	13.28	243	1.93	1.49	29.67	0.47	6.15	98.6
x=0.5	600	264	16.11	70	5.54	0.71	10.31	0.76		
x=1	300	149	11.98	262	1.98	1.41	26.19	0.49	6.17	98.9
x=1	600	269	14.37	74	5.78	0.66	10.65	0.74		
x=1.5	300	152	10.99	261	2.18	1.37	28.33	0.47	6.16	98.7
x=1.5	600	276	12.60	75	6.51	0.62	11.41	0.71		
x=2	300	159	9.92	274	2.18	1.31	27.87	0.47	6.14	98.4
x=2	600	283	11.65	76	6.51	0.59	11.16	0.72		
x=3	300	170	8.03	276	2.83	1.26	31.21	0.46	6.11	97.9
x=3	600	290	10.43	75	8.10	0.58	12.02	0.70		
x=4	300	185	6.49	295	3.29	1.16	30.41	0.46	6.12	98.1
x=4	600	299	7.48	79	10.47	0.56	16.57	0.61		

Table S2. Elastic and thermal properties for $Te_{0.985}Sb_{0.015}$-x%$SmSe_2$ at room temperature, including transverse (v_t), longitudinal (v_l) and average sound velocities (v_s), shear (G), bulk (B) and Young's (E) modulus, Grüneisen parameter (γ), Debye temperature (Θ_D) and the minimal lattice thermal conductivity (κ_{min}).

Composition	v_t (m s^{-1})	v_l (m s^{-1})	v_s (m s^{-1})	G (GPa)	B (GPa)	E (GPa)	γ	Θ_D (K)	Calculated κ_{min} (W m^{-1}K^{-1})
x=0	1447	2462	1604	12.9	20.2	32.0	1.44	148	0.28
x=0.5	1441	2359	1591	12.8	17.2	30.7	1.30	146	0.28
x=1	1429	2473	1586	12.6	20.9	31.5	1.50	146	0.28
x=1.5	1489	2528	1650	13.7	21.2	33.7	1.43	152	0.29
x=2	1448	2320	1596	12.9	15.9	30.4	1.22	147	0.28
x=3	1455	2429	1609	12.9	18.8	31.5	1.37	148	0.28
x=4	1483	2471	1640	13.5	19.4	32.8	1.36	151	0.29

Table S3. Parameters used for the modified Debye-Callaway modeling based on the various phonon scattering mechanisms of Umklapp processes (U), Normal processes (N), grain boundaries (B), point defects (PD), dislocations (D), and Nanostructure interfaces (I) in $Te_{0.985}Sb_{0.015}$-2%$SmSe_2$.

Scattering mechanisms	Relaxation times (τ)	Parameters	Symbol	Values
Umklapp processes	$\tau_U^{-1} = \frac{\hbar\gamma^2 T}{\bar{M} v_s^2 \Theta_D} \omega^2 e^{-\Theta_D/3T}$	Grüneisen parameter	γ	1.22
		Average atomic mass	$\bar{M}$ (kg)	2.11×10^{-25}
		Average sound velocity	v_s (m s^{-1})	1596
	$v_s = \left(\frac{1}{3}\left[\frac{2}{v_t^3} + \frac{1}{v_l^3}\right]\right)^{-1/3}$	Longitudinal sound velocity	v_l (m s^{-1})	2320
		Transverse sound velocity	v_t (m s^{-1})	1448
	$\Theta_D = \frac{h}{k_B}\left[\frac{3N}{4\pi V}\right]^{1/3} v_s$	Debye temperature	Θ_D (K)	147
		Number of atoms in a unit cell	N	3
		Unit-cell volume	V (Å^3)	101.81
Normal processes	$\tau_N^{-1} = \beta\tau_U^{-1}$	Ratio of normal and Umklapp process	β	0.6 (fitted)
Grain boundary	$\tau_B^{-1} = \frac{v_s}{d_{avg}}$	Average grain size	d_{avg} (nm)	1000
Point defects[5]	$\tau_{PD}^{-1} = \frac{\bar{V}\omega^4}{4\pi v_s^3}\Gamma_{(Te,Se)}$	Average atomic volume	$\bar{V}$ (m^3)	3.43×10^{-29}
	$\Gamma_{(Te,Se)} = x(1-x)\left[\left(\frac{\Delta M}{M_{(Te,Se)}}\right)^2 + \varepsilon\left(\frac{\Delta r}{r_{(Te,Se)}}\right)^2\right]$	Point defect scattering parameter	$\Gamma_{(Te,Se)}$	0.016
		Phenomenological parameter	ε	43
	$\Delta M = M_{Te} - M_{Se}$	Mole mass of Te, Se	M_{Te}(g mol^{-1})	127.6
	$M_{(Te,Se)} = (1-x)M_{Te} + xM_{Se}$		M_{Se} (g mol^{-1})	78.9
	$\Delta r = r_{Te} - r_{Se}$	Atomic radius of Te, Se	r_{Te} (Å)	1.35
	$r_{(Te,Se)} = (1-x)r_{Te} + xr_{Se}$		r_{Se} (Å)	1.16
	$\varepsilon = \frac{2}{9}\left[\frac{6.4\times\gamma(1+r)}{1-r}\right]^2$			
Dislocations[7]	$\tau_D^{-1} = \tau_{DC}^{-1} + \tau_{DS}^{-1}$	Dislocation density	N_D (cm^{-2})	1.34×10^{11}
	$\tau_{DC}^{-1} = \frac{N_D \bar{V}^{4/3}}{v_s^2}\omega^3$	Pre-factor of dislocation scattering	A	0.6
	$\tau_{DS}^{-1} = A\times N_D b^2\gamma^2\omega\left\{\frac{1}{2} + \frac{1}{24}\left(\frac{1-2r}{1-r}\right)^2\left[1+\sqrt{2}\left(\frac{v_l}{v_t}\right)\right]^2\right\}$	Burger's vector	b (Å)	2.5 [8]
		Poisson ratio	r	0.18
	$N_D = \frac{2\sqrt{3}\langle\varepsilon^2\rangle^{1/2}}{(d_{avg}\times b)}$	Lattice strain	ε (%)	0.385
Nanostructure interfaces[9]	$\tau_I^{-1} = v_s N_p\left[(2\pi R^2)^{-1} + \left(\frac{4}{9}\pi R^2\left(\frac{\Delta D}{D}\right)^2\left(\frac{\omega R}{v_s}\right)^4\right)^{-1}\right]^{-1}$	Number density of precipitates	N_p (m^{-3})	6.96×10^{23}
		Average radius for the precipitates	R (nm)	2

Matrix density	D (g cm^{-3})	6.14
Density difference between matrix and precipitates	ΔD (g cm^{-3})	0.065

Table S4. Comparison of room-temperature lattice thermal conductivity (κ_L) and average sound velocity for elemental and Te-related thermoelectric semiconductors.

Materials	κ_L (W m^{-1}K^{-1})	v_s (m s^{-1})	References
PbTe	2	1850	[10, 11]
SnTe	2.85	1800	[10, 12]
Ag_8GeTe_6	0.2	1723	[13]
Ag_9TlTe_5	0.22	1203	[14]
$TlSbTe_2$	0.6	1870	[15]
$TlBiTe_2$	1.1	1399	[16]
Bi_2Te_3	1.4	1615	[17, 18]
GeTe	2.8	1900	[10, 19]
Cu_2Te	1.6	1833	[20]
Te	1.65	1611	This work
Sb	5	3145	[21]
Bi	1.9	1712	[21]
Ge	62	3829	[21]
Si	156	6401	[21]
Ag_2Te	0.26	1360	[22]
La_3Te_4	2	2237	[23]
CdTe	7.5	2000	[24]
MnTe	1.2	2180	[25]
$MnTe_2$	1.9	2180	[26]
$AgSbTe_2$	0.6	1727	[27, 28]
Pr_3Te_4	0.78	2147	[29]
ZnTe	18	2210	[30, 31]
BaTe	10	2470	[32, 33]
MgTe	16	2578	[32]
In_2Te_3	–	–	[34]
Ga_2Te_3	0.58	–	[35]
$CuInTe_2$	4.6	1992	[36, 37]
Sb_2Te_3	1.5	2900	[38, 39]
$AgBiTe_2$	0.44	2318	[40]
$CuGaTe_2$	7.5	2364	[41]
CaTe	3.1	2249	[32, 42]
SrTe	2.5	1937	[42]
BeTe	175	4180	[32, 43]
As_2Te_3	0.6	1600	[44]
$CsBi_4Te_6$	0.5	–	[45]
Li_2Te	–	2502	[46]
Rb_2Te	–	1471	[46]
K_2Te	–	1942	[46]
Na_2Te	–	2225	[46]

HgTe	2.4	1763	[21, 47]
InTe	0.75	1394	[48]
$TlInTe_2$	0.63	1707	[49, 50]
$TlGaTe_2$	0.73	1479	[50, 51]
AgTlTe	0.25	1282	[52, 53]
$CuGaTe_2$	7.5	2364	[54]
$CuTl_9Te_5$	0.23	1249	[20]
Tl_2GeTe_3	0.29	1011	[55]
Tl_4SnTe_3	0.29	1428	[55]
Tl_4PbTe_3	0.58	1411	[55]
Tl_2Te	0.34	1136	[20]
Tl_8GeTe_5	0.14	1052	[56]

Composition	T (K)	S (μV K^{-1})	ρ (mΩ cm)	k_{tot} (W m^{-1}K^{-1})	zT	max η_r (%)	s (V^{-1})	u (V^{-1})	η_r (%)	Φ (V)	η (%)	Device ZT
x=2	300	159	2.18	1.51	0.23	5.2	2.29	3.50	3.9	0.3334		
x=2	325	171	2.33	1.38	0.29	6.4	2.48	3.58	5.4	0.3346	0.4	0.21
x=2	350	183	2.51	1.26	0.37	7.8	2.65	3.67	6.9	0.3362	0.8	0.24
x=2	375	195	2.74	1.16	0.45	9.3	2.79	3.78	8.3	0.3379	1.4	0.28
x=2	400	207	3.01	1.06	0.54	10.7	2.89	3.89	9.7	0.3400	1.9	0.32
x=2	425	219	3.33	0.98	0.63	12.1	2.95	4.02	10.9	0.3421	2.6	0.35
x=2	450	231	3.69	0.91	0.71	13.4	2.98	4.16	11.9	0.3444	3.2	0.39
x=2	475	242	4.09	0.85	0.80	14.6	2.97	4.31	12.6	0.3467	3.9	0.42
x=2	500	252	4.54	0.80	0.87	15.6	2.93	4.48	12.8	0.3490	4.5	0.45
x=2	525	261	5.01	0.76	0.94	16.4	2.86	4.67	12.4	0.3512	5.1	0.47
x=2	550	270	5.51	0.73	0.99	17.1	2.78	4.88	11.4	0.3532	5.6	0.48
x=2	575	277	6.01	0.71	1.03	17.6	2.67	5.11	9.5	0.3550	6.1	0.49
x=2	600	283	6.51	0.70	1.06	17.9	2.56	5.37	6.6	0.3562	6.4	0.49

Table S5. The calculation of ZT from device efficiency according to the Snyder's model in $Te_{0.985}Sb_{0.015}$-2%$SmSe_2$ system.

References

[1] Anderson OL. Journal of Physics and Chemistry of Solids 1963;24:909.

[2] Górecki T. Materials Science and Engineering 1980;43:225.

[3] Manikandan M, Amudhavalli A, Rajeswarapalanichamy R, Iyakutti K. Solid State Communications 2019;291:36.

[4] Lin S, Li W, Zhang X, Li J, Chen Z, Pei Y. Inorganic Chemistry Frontiers 2017;4:1066.

[5] An D, Chen S, Lu Z, Li R, Chen W, Fan W, Wang W, Wu Y. ACS applied materials & interfaces 2019;11:27788.

[6] Peng H, Kioussis N, Snyder GJ. Physical Review B 2014;89.

[7] Kim H-S, Kang SD, Tang Y, Hanus R, Jeffrey Snyder G. Materials Horizons 2016;3:234.

[8] Nandi RK, Sen Gupta SP. Thin Solid Films 1979;59:295.

[9] Chen Z, Jian Z, Li W, Chang Y, Ge B, Hanus R, Yang J, Chen Y, Huang M, Snyder GJ, Pei Y. Advanced materials 2017;29.

[10] Bauer Pereira P, Sergueev I, Gorsse S, Dadda J, Müller E, Hermann RP. physica status solidi (b) 2013;250:1300.

[11] Tian Z, Garg J, Esfarjani K, Shiga T, Shiomi J, Chen G. Physical Review B 2012;85.

[12] Al Rahal Al Orabi R, Hwang J, Lin C-C, Gautier R, Fontaine B, Kim W, Rhyee J-S, Wee D, Fornari M. Chemistry of Materials 2016;29:612.

[13] Charoenphakdee A, Kurosaki K, Muta H, Uno M, Yamanaka S. physica status solidi (RRL) – Rapid Research Letters 2008;2:65.

[14] Kurosaki K, Kosuga A, Muta H, Uno M, Yamanaka S. Applied Physics Letters 2005;87:061919.

[15] Kurosaki K, Uneda H, Muta H, Yamanaka S. Journal of Alloys and Compounds 2004;376:43.

[16] Kurosaki K, Kosuga A, Yamanaka S. Journal of Alloys and Compounds 2003;351:14.

[17] Satterthwaite CB, Ure RW. Physical Review 1957;108:1164.

[18] Xie W, Tang X, Yan Y, Zhang Q, Tritt TM. Applied Physics Letters 2009;94:102111.

[19] Li J, Zhang X, Lin S, Chen Z, Pei Y. Chemistry of Materials 2016;29:605.

[20] Kurosaki K, Goto K, Kosuga A, Muta H, Yamanaka S. Materials Transactions 2006;47:1432.

[21] Madelung O.

[22] Pei Y, Heinz NA, Snyder GJ. Journal of Materials Chemistry 2011;21:18256.

[23] May AF, Fleurial J-P, Snyder GJ. Physical Review B 2008;78.

[24] Slack GA, Galginaitis S. Physical Review 1964;133:A253.

[25] Xu Y, Li W, Wang C, Li J, Chen Z, Lin S, Chen Y, Pei Y. Journal of Materials Chemistry A 2017;5:19143.

[26] Xu Y, Li W, Wang C, Chen Z, Wu Y, Zhang X, Li J, Lin S, Chen Y, Pei Y. Journal of Materiomics 2018;4:215.

[27] Amouyal Y. Computational Materials Science 2013;78:98.

[28] Ye L-H, Hoang K, Freeman AJ, Mahanti SD, He J, Tritt TM, Kanatzidis MG. Physical Review B 2008;77.

[29] Cheikh D, Hogan BE, Vo T, Von Allmen P, Lee K, Smiadak DM, Zevalkink A, Dunn BS, Fleurial J-P, Bux SK. Joule 2018;2:698.

[30] Lee BH. Journal of Applied Physics 1970;41:2984.

[31] Slack GA. Physical Review B 1972;6:3791.

[32] Seko A, Togo A, Hayashi H, Tsuda K, Chaput L, Tanaka I. Physical review letters 2015;115:205901.

[33] Tuncel E, Colakoglu K, Deligoz E, Ciftci YO. Journal of Physics and Chemistry of Solids 2009;70:371.

[34] Tsuchiya Y. Journal of the Physical Society of Japan 1988;57:2425.

[35] Kim C-e, Kurosaki K, Ishimaru M, Jung D-y, Muta H, Yamanaka S. physica status solidi (RRL) - Rapid Research Letters 2009;3:221.

[36] Fernández B, Wasim SM. physica status solidi (a) 1990;122:235.

[37] Luo Y, Jiang Q, Yang J, Li W, Zhang D, Zhou Z, Cheng Y, Ren Y, He X, Li X. Nano Energy 2017;32:80.

[38] Narendra N, Kim KW. Semiconductor Science and Technology 2017;32:035005.

[39] Zheng D, Tanaka S, Miyazaki K, Takashiri M. Journal of Electronic Materials 2014;44:1679.

[40] Nielsen MD, Ozolins V, Heremans JP. Energy Environ. Sci. 2013;6:570.

[41] Shen J, Zhang X, Lin S, Li J, Chen Z, Li W, Pei Y. Journal of Materials Chemistry A 2016;4:15464.

[42] Ren Y. Computational Condensed Matter 2017;11:69.

[43] Wagner V, Gundel S, Geurts J, Gerhard T, Litz T, Lugauer HJ, Fischer F, Waag A, Landwehr G, Kruse R, Becker C, Küster

U. Journal of Crystal Growth 1998;184-185:1067.
[44] Vaney JB, Carreaud J, Delaizir G, Morin C, Monnier J, Alleno E, Piarristeguy A, Pradel A, Gonçalves AP, Lopes EB, Candolfi C, Dauscher A, Lenoir B. Journal of Electronic Materials 2015;45:1786.
[45] Chung D-Y, Hogan T, Brazis P, Rocci-Lane M, Kannewurf C, Bastea M, Uher C, Kanatzidis MG. Science 2000;287:1024.
[46] Souadia Z, Bouhemadou A, Khenata R, Al-Douri Y. Physica B: Condensed Matter 2017;521:204.
[47] Whitsett CR, Nelson DA. Physical Review B 1972;5:3125.
[48] Jana MK, Pal K, Waghmare UV, Biswas K. Angewandte Chemie 2016;55:7792.
[49] Jana MK, Pal K, Warankar A, Mandal P, Waghmare UV, Biswas K. Journal of the American Chemical Society 2017;139:4350.
[50] Wu M, Enamullah, Huang L. Physical Review B 2019;100.
[51] Matsumoto H, Kurosaki K, Muta H, Yamanaka S. Journal of Applied Physics 2008;104:073705.
[52] Kurosaki K, Goto K, Muta H, Yamanaka S. Journal of Applied Physics 2007;102:023707.
[53] Kurosaki K, Kosuga A, Muta H, Yamanaka S. MATERIALS TRANSACTIONS 2005;46:1502.
[54] Li W, Lin S, Ge B, Yang J, Zhang W, Pei Y. Advanced science 2016;3:1600196.
[55] Kosuga A, Kurosaki K, Muta H, Yamanaka S. Journal of Applied Physics 2006;99:063705.
[56] Kurosaki K, Kosuga A, Charoenphakdee A, Matsumoto H, Muta H, Yamanaka S. Materials Transactions 2008;49:1728.